ACSNANO

www.acsnano.org

ARTICLE

Properties of DNA- and Protein-Scaffolded Lipid Nanodiscs

Vishal Maingi* and Paul W. K. Rothemund*

Cite This: https://dx.doi.org/10.1021/acsnano.0c07128

Read Online

ACCESS | Metrics & More | Article Recommendations | Supporting Information

ABSTRACT: The properties of natural lipid bilayers are vital to the regulation of many membrane proteins. Scaffolded nanodiscs provide an *in vitro* lipid bilayer platform to host membrane proteins in an environment that approximates native lipid bilayers. However, the properties of scaffold-enclosed bilayers may depart significantly from those of bulk cellular membranes. Therefore, to improve the usefulness of nanodiscs it is essential to understand the properties of lipids restricted by scaffolds. We used computational molecular dynamics and modeling approaches to understand the effects of nanodisc size, scaffold type (DNA or protein), and hydrophobic modification of DNA scaffolds on bilayer stability and degree to which the properties of enclosed bilayers approximate bulk bilayers. With respect to achieving bulk bilayer behavior, we found that charge neutralization of DNA scaffolds was more important than the total hydrophobic content of their modifications: bilayer properties were better for scaffolds having a large number of short alkyl chains than those having fewer long alkyl chains. Further, complete charge neutralization of DNA scaffolds enabled better lipid binding, and more stable bilayers, as shown by steered molecular dynamics simulations that measured the force required to dislodge scaffolds from lipid bilayer patches. Considered together, our simulations provide a guide to the design of DNA-scaffolded nanodiscs suitable for studying membrane proteins.

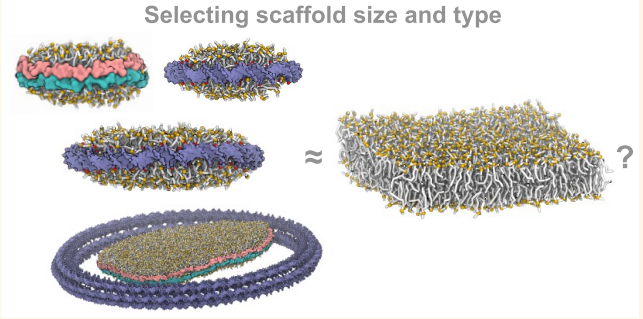

KEYWORDS: *nanodiscs, lipid−DNA interaction, lipid−protein interaction, membrane scaffolds, computational design, molecular dynamics, DNA origami*

Membrane proteins govern many processes vital to biological function, such as cellular communication and transport across the membrane.[1] Membrane proteins are an enormously important class of proteins, yet they are poorly understood because it is difficult to study them in their native environment. Nanodiscs are water-soluble lipid bilayer patches secured by amphipathic scaffolds (containing both hydrophobic and hydrophilic functional groups), which can serve as a platform to host membrane proteins. Nanodisc scaffolds are necessary to secure and stabilize lipid bilayer patches in an aqueous solution: the scaffold provides a stable belt around the membrane proteins and lipids, makes the whole assembly soluble, and its length determines the size of the disc. *In vitro* nanodisc platforms are useful for studying isolated membrane proteins, in a native lipid environment. In many cases, this may be advantageous over an *in vivo* environment, *e.g.*, because isolated proteins can be studied without the crowding effects of other proteins.

When using nanodiscs, a variety of experimental methodologies can be employed to understand a range of structural and functional properties of membrane proteins.[2,3] Some studies suggest that lipid bilayers, and their resulting properties, act as "allosteric" regulators of membrane protein function.[4] For example, catalytic,[5] transport,[6] and thermosensation[7,8] properties of membrane proteins are affected by lipid types and their dynamics.[9] Some simple properties such as bilayer thickness and lipid order parameter are known to affect membrane proteins.[4] In general, the lipid order parameter describes the conformational arrangement of acyl chain atoms (C−C, C−H)[10,11] or acyl chain coarse-grained beads[12] with respect to the lipid bilayer normal. Lipid bilayer composition is known to affect the lipid order parameter, which can in turn influence membrane protein properties. For example, the kinetics of metarhodopsin formation are known to be dependent on cholesterol-induced lipid ordering.[13] While nanodiscs provide a lipid environment,

Received: August 24, 2020
Accepted: December 1, 2020

the boundary condition defined by the scaffold may create a variety of unnatural artifacts. Thus, it is important to understand how the scaffold and its associated features (such as the size or chemistry) affect lipid properties, behavior, and eventual downstream allosteric protein regulation.

Protein[14] scaffolds for nanodiscs have been used since 2002, and their utility has increased as more versatile versions have been developed. A review by Pourmousa and Pastor[15] explores developments in the structure and modeling of protein scaffold nanodiscs. In general, full-length linear protein scaffolds are highly dynamic; truncated versions have been developed to help to reduce fluctuations near terminal domains.[15] Alternatively, when covalently circularized protein scaffolds are used, more thermally stable nanodiscs of more consistent diameter are formed.[16] In addition to protein scaffolds, polymer,[17] DNA,[18] and hybrid DNA−protein[19] scaffolds have also been used to assemble lipid bilayer nanodiscs. DNA scaffolds have further been used to pattern lipids into spherical liposomes or tubular forms,[20,21] to introduce curvature[22] at the membrane surface, and to create geometric arrangements of small protein nanodiscs.[23] Nanodiscs are available in a range of diameters, from 6.3 nm[2,24] to 70 nm.[19] Larger nanodiscs might be expected to have membrane properties that are more representative of natural bulk membranes, but because they are expensive and difficult to make, the choice of nanodisc in any given laboratory experiment is typically driven by the size of the transmembrane domain of the protein being studied. Here, one of the hypotheses we wish to investigate is that larger nanodiscs may have better properties. Because the largest experimentally reported nanodiscs have featured DNA−protein hybrids,[19] and because techniques used to create small nanodiscs from DNA-only scaffolds[18] might be extended to larger sizes, we decided to explore a range of nanodiscs based on protein, DNA, or hybrid protein/DNA scaffolds.

Many different nanodisc scaffold types share a common feature: the presence of an inner belt of hydrophobic residues that helps establish favorable interactions with lipid acyl tails. In general, amphipathic protein scaffolds contain inner-facing hydrophobic amino acid side chains. For DNA-based constructs, alkyl,[18,25] cholesterol,[26] or porphyrin[27] modifications have been used to create hydrophobicity on their surface. Based on their pK_a, the chemical moieties in the vicinity of hydrophobic residues are either charged or neutral. These differing chemical moieties help explain why nanodiscs enclosed by different types of scaffolds can yield bilayers with membrane properties that depart from those of a scaffold-free bilayer (bulk membrane). Because lipid properties are known to be allosteric modulators of many membrane proteins,[4] it is essential to know how scaffold size, chemical character, and distribution of hydrophobic residues affect the properties of a nanodisc's bilayer. Such knowledge can inform the design of nanodisc scaffolds: an ideal scaffold would yield nanodiscs with properties similar to that of bulk membrane, and with high stability, so that they can be readily synthesized and studied in the laboratory. For DNA scaffold nanodiscs, we wished to understand whether simple total hydrophobic content was a good predictor of scaffold performance or whether charge neutralization of the DNA backbone was also important.

Computational molecular dynamics (MD) simulation approaches at all-atom[28−33] and coarse-grained (CG) resolutions[28,31] are powerful tools for understanding complex systems such as nanodiscs at the molecular level, when this level of detail is either difficult or impossible to achieve *via* laboratory experiments. For example, while some experimental crystal and solution structural data for scaffold proteins such as apolipoprotein A-1 (APOA1)[34−36] exist, the dynamic nature of APOA1 helices[15] makes it difficult to experimentally resolve important structural features. In the case of DNA-scaffolded nanodiscs, no high-resolution structures exist. One experimental study[18] of 15 nm double-stranded DNA (dsDNA)-scaffolded nanodiscs includes CG MD simulations, but simulated nanodiscs featured a different hydrophobic modification (dodecyl groups) than those of experimental nanodiscs (ethyl, butyl, and decyl groups), and the membrane properties were not analyzed. Thus, to date, the detailed properties of DNA-scaffolded nanodiscs have not been studied with CG MD nor compared with similar protein-scaffolded nanodiscs.

Here, we report our study of lipid bilayer membranes reconstituted with proteins-, DNA-, and hybrid DNA−protein-based scaffolds. To understand the properties and stability of lipid bilayers reconstituted with different scaffolds, we performed MARTINI[37]-based CG-level MD simulations on reported experimental scaffold designs.[16,18,19] We chose CG-level MD because it allows protein/lipid[38] or DNA/lipid[18,39] interactions to be studied over longer time scales. This is an approach that we have found useful in previous studies,[39,40] where it gave insights regarding the stability of hydrophobically modified DNA nanopores in a surrounding lipid bilayer. In the current study, we compare phospholipid bilayers surrounded by a variety of DNA and protein scaffolds and report the effects of (a) nanodisc size, (b) scaffold type, (c) hydrophobic modifications, and (d) scaffold charge density on the properties and stability of the enclosed lipid bilayers. We performed simulations on time scales up to microseconds, with system sizes varying from *ca.* 31 000 to 4.2 million particles depending on nanodisc diameter. We measured the bilayer thickness and lipid order parameter of simulated nanodisc lipid bilayers and determined which scaffold chemistries and diameters gave bilayer properties most similar to that of bulk membranes. Some nanodiscs were stable over the course of the entire CG MD simulation. For some scaffold designs, bilayers partially or completely spontaneously dislocated from their scaffolds; we hypothesize that the degree of stability in CG MD may correspond to the yield of experimental nanodiscs. For CG MD-stable nanodiscs, we used steered molecular dynamics (SMD) simulations to measure the maximum force required to separate the supporting scaffolds from the lipid membrane patches, which we hypothesize could be used as a second surrogate for nanodisc stability. Overall, our simulations allowed us to evaluate a variety of designs inspired by existing experiments and to suggest experimentally achievable improvements for DNA scaffold designs.

RESULTS AND DISCUSSION

Below we organize our study of two membrane properties (thickness and order parameter) based on the size of nanodiscs, exploring scaffolds of increasing diameter, from 11 to 45 nm. For most cases, bilayers were built with palmitoyl-oleoyl-phosphocholine (POPC) since it is widely used both for experimental protein nanodiscs and for CG simulations of membranes; for a couple control simulations, dilauroyl phosphocholine (DLPC) was used. The lipid loading (the number of lipids added in each case) was based on the area defined by the inner diameter of the scaffold. Typically, lipids were added to achieve a standard area per lipid (APL) of 0.683 nm^2 for POPC and a standard APL of 0.641 nm^2 for DLPC. To examine the effects of lipid loading, we

https://dx.doi.org/10.1021/acsnano.0c07128
ACS Nano XXXX, XXX, XXX−XXX

performed some control simulations where the number of lipids was increased or decreased up to 20% relative to that calculated using standard APLs. We explain how and why we chose each model and its relationship to the experimental literature and propose scaffold designs that might be better. Membrane stability is treated at the end in its own section; because of the computational costs of SMD, we consider stability only for 11 nm nanodiscs. Model building for all the scaffolds is described in Supplementary Methods (Model Building). DNA scaffold models (without lipid bilayers) showing hydrophobic alkyl modifications are presented in Figure 1. In all figures, CG water and CG ions are hidden for clarity. Table 1 summarizes details for all simulations.

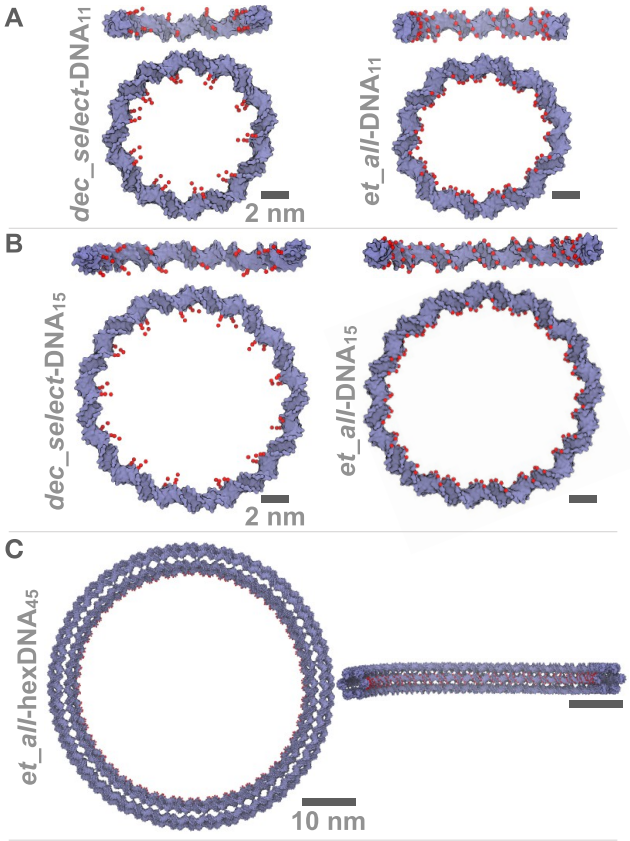

Figure 1. Hydrophobic modifications on DNA scaffolds. Hydrophobic alkyl modifications on DNA scaffolds shown for (A) 11 nm nanodiscs: selectively decylated *dec_select*-DNA$_{11}$ with 20 decyl chains (left) and fully ethylated *et_all*-DNA$_{11}$ with 85 ethyl chains (right), (B) *dec_select*-DNA$_{15}$ with 26 decyl chains (left) and *et_all*-DNA$_{15}$ case with 119 ethyl chains (right), and (C) *et_all*-hexDNA$_{45}$ case with 360 ethyl modifications. In all cases top views and cross sections are shown. DNA, blue surface; decyl in A, B/ethyl in A, B, C, red beads.

11 nm Protein- and DNA-Scaffolded Nanodiscs. Covalently circularized protein scaffold-based nanodiscs have been reported experimentally,[16] and these nanodiscs were found to be 5 °C more thermally stable than their open, linearized forms in melting experiments. Thus, we first compared an 11 nm diameter nanodisc scaffolded by a covalently circularized protein (circNW$_{11}$, Figure 2A; NW stands for nanodisc width), to a nanodisc scaffolded by its linearized form (NW$_{11}$; Supplementary Figure S2A) and found that our methods (at CG resolution) could not distinguish between them with respect to membrane properties.

More interesting were simulations comparing circNW$_{11}$ to a pair of nanodiscs scaffolded by closed dsDNA rings, which captured both potential differences between protein and DNA scaffolds and the potential importance of charge neutralization relative to total hydrophobic content. Experimentally reported dsDNA scaffolds[18] were *ca.* 15 nm in diameter and were modified with either ethyl (2 carbon), butyl (4 carbon), or decyl (10 carbon) chains. Among these different scaffold designs, the decyl-modified scaffold was the most hydrophobic, and so we expected it to have the best lipid binding; thus for our first dsDNA ring model we used a decyl-modified design. Later we present a model that better approximates the experimental 15 nm dsDNA ring; however here, to enable more direct comparison with circNW$_{11}$, we modeled an 11 nm dsDNA ring (*dec_select*-DNA$_{11}$, Figure 2B) having almost the same density of hydrophobic groups as the 15 nm ring, with 4 decyl groups per 21 nucleotides of scaffold, for a total of 20 modifications and a total hydrophobic content of 200 carbon atoms.

This selectively decylated model, *dec_select*-DNA$_{11}$, has DNA backbone phosphates that are neutral at the site of decyl modifications; the rest of the DNA backbone phosphate groups remain negatively charged and a large number of these phosphates (*ca.* 65 sites) face inward toward the bilayer (*ca.* 13 remnant charges per 21 nucleotide base pairs of scaffold). We knew from our previous MD studies[39] that DNA nanopore–lipid wetting (immediate membrane thickness around the DNA pore) is related to the length of the completely neutral hydrophobic belt along the pore (with zero charged sites), which in those simulations was implemented by shorter ethyl modifications. We thus decided to construct a model having similar (slightly lower) hydrophobic content but with complete charge neutralization, having inward-facing zero charged backbone sites: the "fully ethylated" *et_all*-DNA$_{11}$ (Figure 2C), which has a total of 85 modifications and a total hydrophobic content of 170 carbon atoms, providing a complete neutral and hydrophobic inner belt that is *ca.* 2 nm thick.

Membrane properties for simulated POPC-filled nanodiscs based on the scaffolds circNW$_{11}$, *dec_select*-DNA$_{11}$, and *et_all*-DNA$_{11}$ were compared to each other and to the properties of simulated bulk POPC membrane as a reference (Supplementary Figure S4); each case was simulated for 1 μs and repeated four times. We first examined membrane thickness (Figure 3A and Supplementary Methods, Analyses), where, for each grid box, thickness was calculated as the distance between the density peaks of lipid phosphate head groups binned along the z direction (perpendicular to the xy plane of the nanodisc). The colormap was chosen arbitrarily to highlight features of lipid thickness, as a function of radial distance from the center, and relative to the simulated bulk thickness. For example, bulk thickness is *ca.* 3.8 nm (in good agreement with experiments[41,42] and CG Martini models[43]), and we colored 4 nm thickness cyan, so that thicknesses close to the bulk thickness are easily recognized.

We make some observations that hold in all cases. First, the bilayer proximal (within 1 nm along a radius) to the DNA or protein scaffold is significantly thinned (<1 nm thick); here lipid head groups can make idiosyncratic and persistent contacts with features of the scaffold, as is apparent for head groups binding in the major groove of the DNA scaffolds (zoom-ins Figure 2B,C). Moving closer to the center, there is a smooth increase in

https://dx.doi.org/10.1021/acsnano.0c07128
ACS Nano XXXX, XXX, XXX−XXX

Table 1. Summary of All the MD Simulations Conducted in This Study[a]

simulation	hydrophobic group	duration (repeats × time)	internal diameter in nm (*number of lipids calculated to fit in internal area*), **lipids actually inserted**	relative remarks and properties compared to bulk POPC[c]
ca. 11 nm Nanodiscs				
circNW$_{11}$ (Figure 2A)	amino acids[b]	4 × 1 μs	8.9 (*92*), **91**	membrane stable; lipid properties poor
$^{-10\%}$circNW$_{11}$ (Supplementary Figure S5A)		2 × 1 μs	8.9 (*92*), **82**	
$^{+10\%}$circNW$_{11}$ (Supplementary Figure S7A)		2 × 1 μs	8.9 (*92*), **100**	
NW$_{11}$ (Supplementary Figure S2A)	amino acids[b]	4 × 1 μs	8.9 (*92*), **91**	membrane stable; lipid properties poor
dec_select-DNA$_{11}$ (Figure 2B)	decyl (select residues[b])	4 × 1 μs	8.9 (*92*), **91**	membrane stable; lipid properties poor
$^{-10\%}$*dec_select*-DNA$_{11}$ (Supplementary Figure S5B)		2 × 1 μs	8.9 (*92*), **82**	membrane stable; lipid properties poor
$^{+10\%}$*dec_select*-DNA$_{11}$ (Supplementary Figure S7B)		2 × 1 μs	8.9 (*92*), **100**	membrane not stable
et_all-DNA$_{11}$ (Figure 2C)	ethyl (all inner residues)	4 × 1 μs	8.9 (*92*), **91**	membrane stable; lipid properties poor
$^{-10\%}$*et_all*-DNA$_{11}$ (Supplementary Figure S5C)		2 × 1 μs	8.9 (*92*), **82**	
$^{+10\%}$*et_all*-DNA$_{11}$ (Supplementary Figure S7C)		2 × 1 μs	8.9 (*92*), **100**	
ca. 15 nm Nanodiscs				
dec_select-DNA$_{15}$ (Figure 4A)	decyl (select residues[b])	4 × 1 μs	13.1 (*197*), **197**	membrane stable; lipid properties poor
et_all-DNA$_{15}$ (Figure 4B)	ethyl (all inner residues on both DNA strands)	4 × 1 μs	13.1 (*197*), **195**	membrane stable; lipid properties better
et_ss-DNA$_{15}$ (Supplementary Figure S9)	ethyl (all inner residues on one of two DNA strands)	2 × 1 μs	13.1 (*197*), **198**	membrane not stable
et_select-DNA$_{15}$ (Supplementary Figure S9)	ethyl (select residues[b])	2 × 1 μs	13.1 (*197*), **199**	membrane not stable
$^{-10\%}$*et_select*-DNA$_{15}$ (Supplementary Figure S10)		2 × 1 μs	13.1 (*197*), **178**	
$^{-20\%}$*et_select*-DNA$_{15}$ (Supplementary Figure S10)		2 × 1 μs	13.1 (*197*), **160**	
$^{+10\%}$*et_select*-DNA$_{15}$ (Supplementary Figure S10)		2 × 1 μs	13.1 (*197*), **220**	
$^{+20\%}$*et_select*-DNA$_{15}$ (Supplementary Figure S10)		2 × 1 μs	13.1 (*197*), **239**	
ca. 45 nm Nanodiscs				
et_all-hexDNA$_{45}$ (Figure 6A)	ethyl (all inner residues)	1 × 1 μs	43.3 (*2157*), **2155**	membrane stable; lipid properties good
hexDNA::NW$_{11}$ (Figure 6B)	amino acids[b]	1 × 1 μs	38.6 (*1714*), **1723**	membrane stable; lipid properties good
hexDNA:NW$_{11}$ (Figure 6C)	amino acids[b]	1 × 0.5 μs	38.6 (*1714*), **1723**	membrane stable; lipid properties good
et_all-DNA$_{45}$ (Supplementary Figure S12)	ethyl (all inner residues)	1 × 1 μs	43.2 (2146), **2149**	membrane stable
Steered MD				
SMD-circNW$_{11}$ (Figure 8)	amino acids[b]	*10* nm μs^{-1}; 4 × 1 μs	8.9 (*92*), **91**	highest maximum force[d]
SMD-*dec_select*-DNA$_{11}$ (Figure 8)	decyl (select residues[b])	*10* nm μs^{-1}; 3 × 1 μs,1 × 0.6 μs	8.9 (*92*), **91**	lowest maximum force[d]
$^{-10\%}$SMD-*dec_select*-DNA$_{11}$ (Supplementary Figure S13)		*10* nm μs^{-1}; 2 × 0.8 μs,	8.9 (*92*), **82**	maximum force reduced
SMD-*et_all*-DNA$_{11}$ (Figure 8)	ethyl (all inner residues)	*10* nm μs^{-1}; 4 × 1 μs	8.9 (*92*), **91**	high maximum force[d]
$^{-10\%}$SMD-*et_all*-DNA$_{11}$ (Supplementary Figure S13)		*10* nm μs^{-1}; 2 × 0.8 μs,	8.9 (*92*), **82**	maximum force is high
$^{+10\%}$SMD-*et_all*-DNA$_{11}$ (Supplementary Figure S13)		*10* nm μs^{-1}; 2 × 0.8 μs,	8.9 (*92*), **100**	maximum force increased
Other cases				
POPC bilayer (bulk)	N.A.	4 × 1 μs	N.A. (*N.A.*), **576**	represents bulk bilayer case
dec_select-DNA$_{15}$[DLPC] (Supplementary Figure S11)	decyl (select residues[b])	4 × 1 μs	13.1 (*211*), **214**	membrane stable
et_all-DNA$_{15}$[DLPC] (Supplementary Figure S11)	ethyl (all inner residues)	4 × 1 μs	13.1 (*211*), **213**	membrane stable

[a]POPC lipid was used in all the cases, except where a different lipid is explicitly mentioned (*e.g.*, [DLPC]). Note that for *et_all*-hexDNA$_{45}$, 45 nm refers to an approximate diameter of the innermost dsDNA helix in a six-helix bundle arrangement (Supplementary Methods and Figure 1C). For abbreviations see text. Unless otherwise stated, the number of lipids added per layer is equal to the scaffold area (from the internal diameter of the scaffold) divided by an area per lipid (APL) of 0.683 nm^2 for POPC and 0.641 nm^2 for DLPC. Labels ±10% or ±20% indicate an introduction of

https://dx.doi.org/10.1021/acsnano.0c07128
ACS Nano XXXX, XXX, XXX−XXX

Table 1. continued

10% or 20% more or less lipids relative to that calculated using standard APL. [b]Our choice of hydrophobic residues and their positions on the scaffold were based on reported experimental designs. [c]Bulk refers here to the pure POPC bilayer case with no scaffold (Supplementary Figure S4). Lipid bilayer membrane properties refer to observed membrane thickness and lipid order parameter. "Poor" refers to nanodisc lipid properties far from bulk properties. Better/good refers to nanodisc lipid properties closer to bulk properties. [d]Comparing the cases where lipid content (number lipids) is the same.

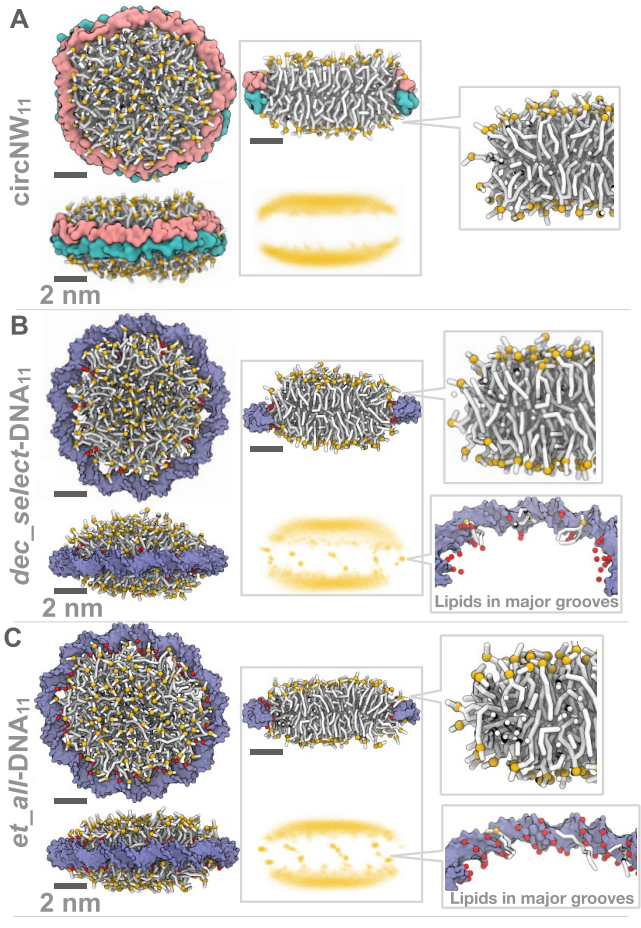

Figure 2. Simulation of 11 nm scaffolds with POPC bilayers. (A) Left panel: Top and side views of circNW$_{11}$ showing a protein double-belt scaffold (pink, cyan) securing a patch of POPC lipid bilayer. (B) Left panel: Top and side views of the selectively decylated *dec_select*-DNA$_{11}$ case showing a dsDNA scaffold (blue surface), modified with decyl chains (red beads). (C) Left panel: Top and side views of fully ethylated *et_all*-DNA$_{11}$ showing a dsDNA scaffold (blue surface), modified with ethyl chains (red beads). Center panels (A, B, and C): Top cross sections show lipid−DNA/protein scaffold interaction in a single simulation frame; bottom cross sections show lipid phosphate head groups only (orange dots), for a superposition of over a thousand frames extracted from equilibrated trajectory. Right panels (A, B, and C): Zoomed-in cross section of lipids in immediate contact with protein/DNA scaffold (hidden). For DNA scaffolds binding modes of lipids in the major groove are also shown. See Supplementary Figure S3 for number density distribution of lipid head groups around the DNA backbone. Here, POPC lipid tails are represented with white stick models and phosphate head groups as orange spheres. Snapshots are final configurations obtained at 1 μs.

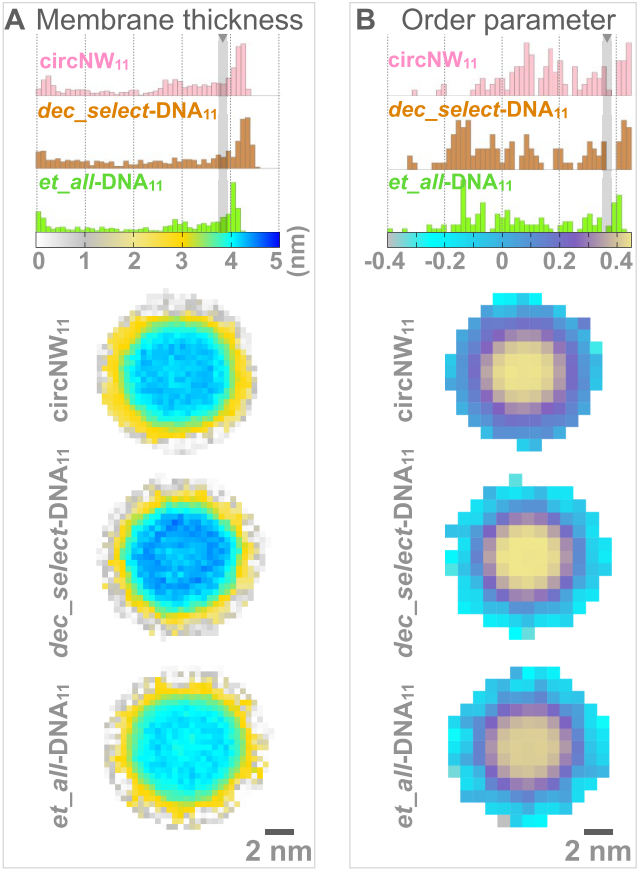

Figure 3. Lipid properties of 11 nm nanodiscs from Figure 2. Top: Normalized histograms (50 bins) of bilayer thickness (A) and order parameter (B) allow comparison of nanodisc membrane properties to those of bulk POPC bilayer, indicated by a gray bar with a black pointer (3.8 nm thickness in A; 0.372 order parameter in B, Supplementary Figure S4). Bottom: *xy* heat map grid plots for POPC bilayer thickness (A) and lipid order parameter (B). For bilayer thickness, grid boxes were 0.4 × 0.4 nm^2; for order parameter, 1 × 1 nm^2). Thickness and order parameter were calculated as described in the text. For both properties, an average over four repeats of each simulation is presented.

membrane thickness, and the bulk thickness (aquamarine/cyan) is reached within 2−3 nm of the nanodisc edge. This is followed by an overshoot of membrane thickness (dark blue) above that of the bulk bilayer and a recovery to a value closer to (but not quite) bulk thickness in the center of the membrane. Similar membrane thinning at nanodisc edges and membrane thickening toward nanodisc centers have been observed in previously reported MD simulations.[30,31] For all cases, most of the bilayer area does not have a thickness that is similar to that of the bulk POPC bilayer, but the most frequently observed thickness (peak of the histogram) is a thickness that is within 0.6 nm of the bulk bilayer thickness.

With respect to specific cases and comparisons, the thickness (at the histogram peak) for our protein nanodisc circNW$_{11}$(4.25 nm) is close (within 8%) but does not quite match the thickness (4.6 nm) observed for similarly sized protein/POPC nanodiscs in SAXS experiments.[44] With respect to matching the thickness of bulk POPC (3.8 nm), the fully ethylated *et_all*-DNA$_{11}$ is best (4.1 nm peak thickness), followed by the protein circNW$_{11}$(4.25

https://dx.doi.org/10.1021/acsnano.0c07128
ACS Nano XXXX, XXX, XXX−XXX

nm), followed by the selectively decylated *dec_select*-DNA$_{11}$ (4.5 nm). Gross morphology supports the idea that *dec_select*-DNA$_{11}$ is less similar to bulk POPC and perhaps less stable. In contrast to circNW$_{11}$ (Figure 2A) and ethylated *et_all*-DNA$_{11}$ (Figure 2C), which show relatively flat bilayers that are symmetrically oriented relative to their scaffolds, the bilayer of *dec_select*-DNA$_{11}$ (Figure 2B) has a rounded, lenticular shape, and its plane is slightly tilted relative to that of the scaffold, indicating partial dislocation.

Calculations of the order parameter show trends similar to thickness (Figure 3B and Supplementary Methods, Analyses). The second-rank order parameter was calculated using the relation $P_2 = 0.5(3\cos^2\langle\theta\rangle - 1)$, where θ is the angle between the lipid bilayer normal and the bond direction (coarse-grained bead−bead bond). $P_2 = 1$ indicates perfect alignment of the bond with the bilayer normal, $P_2 = -0.5$ would mean anti-alignment perpendicular to the normal, and $P_2 = 0$ corresponds to a random state. The nanodisc formed by *et_all*-DNA$_{11}$ has an order parameter (0.4 at the histogram peak) closest to that of the bulk POPC (*ca.* 0.372). Bilayer order parameters for circNW$_{11}$ (0.41) and *dec_select*-DNA$_{11}$ (0.43) were both significantly higher. In all cases, lipids were still much less ordered than the bulk membrane (<0.25) at significant distances from the scaffold (up to 3 nm), suggesting that proteins in these nanodiscs would not experience a native environment near the scaffold.

Our simulations of nanodiscs and the observed bilayer properties depend on the assumption that we have chosen an appropriate lipid loading; that is, we have put an appropriate number of lipids into each nanodisc, as a function of its size and type. Ideally one would use a number of lipids drawn from an experimental measurement; here we calculate lipid number using an APL for POPC that is consistent with SAXS measurements of protein-scaffolded nanodiscs.[44] This number may not be appropriate for DNA-scaffolded nanodiscs, but for them data are unavailable. In principle, APLs, or direct numbers of lipids, could be derived from simulations of a nanodisc assembly, starting from empty scaffolds and dissociated lipids. However, such simulations are computationally very expensive, requiring many repeats and many microseconds of simulation time for even small nanodiscs. Even after several microseconds the scaffold-bilayer assembly may not be complete,[28] and thus here we opt to study the effects of lipid over- or underloading by simulating 11 nm nanodisc systems for which the number of enclosed lipids was increased or decreased by 10% compared to that given by our standard APL (Supplementary Figures S5 and S7). In general, we noticed that reducing the lipids by 10% preserved the previously observed qualitative bilayer properties, but that lipid properties were all slightly closer to that of the bulk bilayer ($^{-10\%}$circNW$_{11}$, $^{-10\%}$*dec_select*-DNA$_{11}$, $^{-10\%}$*et_al*-DNA$_{11}$, Supplementary Figure S6) with $^{-10\%}$*et_all*-DNA$_{11}$ exhibiting properties nearly that of the bulk bilayer. Increasing the lipids by 10% slightly worsens the membrane properties for $^{+10\%}$circNW$_{11}$, and $^{+10\%}$*et_all*-DNA$_{11}$ (Supplementary Figure S8), but both nanodiscs remained stable. In the case of $^{+10\%}$*dec_select*-DNA$_{11}$ the bilayer was not stable, it dislodged from the scaffold (Supplementary Figure S7B), and thus membrane properties were not measured, providing a second piece of evidence that charge neutrality, rather than total hydrophobic content, results in better DNA-scaffolded nanodiscs.

We note that determining the best lipid loading for a simulation is, in general, difficult. For example, from the point of view of predicting experimental nanodisc structure, $^{+10\%}$circNW$_{11}$'s maximum thickness of 4.5 nm matched an experimentally reported nanodisc thickness of 4.6 nm[44] better than did simulations at standard or −10% lipid loading. We note, however, that the very same experimental data (APL) were used to derive the standard lipid loading for POPC. If this discrepancy were systematic and extended to DNA scaffolds, we might expect that all of our thicknesses at standard APL-based lipid loading are slight underestimates for what might be expected in experiments. But *a priori* there is no reason to believe that results calibrated or adjusted to match those of protein nanodiscs will generalize perfectly to DNA-scaffolded nanodiscs; ideally experiments on DNA-scaffolded nanodiscs would be used to calibrate DNA-scaffolded nanodisc simulations. Neither can the degree to which simulations match bulk character be used as a perfect guide. While decreasing lipid loading by 10% does slightly improve membrane properties relative to bulk POPC, we will show later that by SMD (Supplementary Figure S13) such a decreased loading may sometimes decrease the stability of lipid-scaffold interactions in the case of DNA nanodiscs. In real experiments, it may be that the nanodiscs that are observed are simply the more stable ones, and thus they might have higher lipid loadings and worse membrane properties, on average. Overall, we believe that simulations are best used to generate or test hypotheses regarding trends in lipid properties rather than making high-precision quantitative predictions. For this purpose, given that it is derived from protein-scaffolded nanodisc experiments and gives a membrane thickness within 8% of that observed in those experiments, our standard APL is a reasonable lipid loading for our simulations.

Our simulations so far highlight two conclusions. First, suitably modified DNA scaffolds (*i.e.*, *et_all*-DNA$_{11}$) can potentially provide a more native lipid environment (with better properties) than a common protein scaffold (circNW11). Second, for small nanodiscs, a scaffold with slightly lower total hydrophobic content and total charge neutralization (*et_all*-DNA$_{11}$) can provide a significantly more native and potentially more stable bilayer than can a scaffold that has greater hydrophobic content but significant remnant backbone charge (*dec_select*-DNA$_{11}$). We remark that only the central <2 nm diameter region (about 4% of the total area) of the nanodisc scaffold by *et_all*-DNA$_{11}$ has properties closely matching that of bulk POPC.

15 nm DNA-Scaffolded Nanodiscs. To study the effects of DNA scaffold size, while maintaining similar chemical properties, we extended our simulations to dsDNA ring scaffolds 15 nm in diameter, which are more directly comparable to recently reported experimental dsDNA scaffold designs.[18] We modeled a 15 nm dsDNA ring with decyl modifications of approximately 4 decyl per 21 nucleotides (*dec_select*-DNA$_{15}$; with $26 \times 10 = 260$ carbon atoms, Figure 4A) and another fully ethylated 15 nm dsDNA ring with a completely neutral inner belt (*et_all*-DNA$_{15}$; $119 \times 2 = 238$ carbon atoms, Figure 4B). Results were broadly similar to those for analogous 11 nm nanodiscs: significant bilayer thinning was observed near the scaffold, and bilayer thickness increased until it overshot (significantly in decylated case) that of bulk POPC thickness. Significant lipid disordering was again observed up to 3 nm from the scaffold. The selectively decylated scaffold again exhibited mild dislocation from the bilayer. The fully ethylated scaffold again had much better lipid properties, with essentially bulk bilayer properties (both for thickness and lipid order) within a 4 nm diameter region at its center (about 9% of the total area). In contrast, the selectively decylated scaffold achieved bulk-like bilayer properties only in a

https://dx.doi.org/10.1021/acsnano.0c07128
ACS Nano XXXX, XXX, XXX−XXX

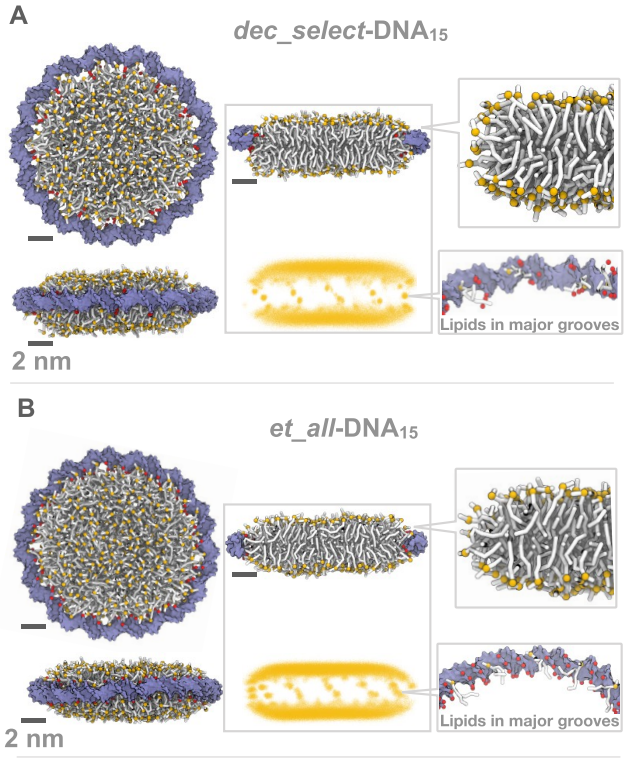

Figure 4. Simulation of 15 nm scaffolds with POPC bilayers. Left panel: Top and side views of final configurations (at 1 μs) for lipid bilayers held by 15 nm dsDNA nanodiscs (A) selectively decylated *dec_select*-DNA$_{15}$ and (B) fully ethylated *et_all*-DNA$_{15}$. Color scheme and middle panels as in Figure 2. See Supplementary Figure S3 for number density distribution of lipid head groups around the DNA backbone.

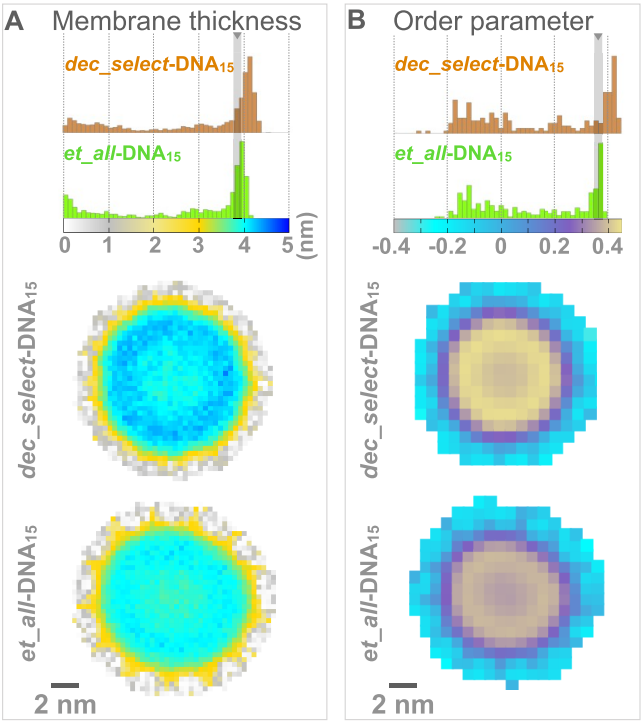

Figure 5. Lipid properties of 15 nm nanodiscs. Normalized histograms of bilayer thickness (A) and order parameter (B) for selectively decylated *dec_select*-DNA$_{15}$ and fully ethylated *et_all*-DNA$_{15}$ are presented at the top. Heat map grid plots are presented at the bottom. All calculations were as in Figure 3.

region <1 nm diameter in its center (<1% of the total area). We observe that thickness profiles and lipid ordering for both *dec_select*-DNA$_{15}$ and *et_all*-DNA$_{15}$ are quite similar near the scaffold, and yet the behavior many nanometers away from the scaffold is still distinct. This suggests that the nature of the scaffold (charge and hydrophobicity) can have indirect, long-range effects on lipid properties.

No fully ethylated scaffolds have been reported, but selectively ethylated scaffolds with low modification density have been reported[18] and found to form nanodiscs in lower yields than an experimental scaffold corresponding to *dec_select*-DNA$_{15}$. We decided to explore the properties of two additional 15 nm ethylated scaffolds that were less than fully ethylated: very low hydrophobicity/high residual backbone charge *et_select*-DNA$_{15}$, with approximately 2 ethyl per 21 nucleotides ($14 \times 2 = 28$ carbon atoms, Supplementary Figure S9A, left), corresponding to the low-yield experimental design;[18] and intermediate hydrophobicity/intermediate residual backbone charge *et_ss*-DNA$_{15}$ ($60 \times 2 = 120$ carbon atoms, Supplementary Figure S9A, right; where "ss" single strand indicates that only one of the two strands of the helix bears modifications). Neither scaffold produced stable nanodiscs; by the end of the simulation *et_select*-DNA$_{15}$ was almost fully dislocated from the nanodisc (Supplementary Figure S9B, left) and *et_ss*-DNA$_{15}$ was significantly tilted relative to the nanodisc (Supplementary Figure S9B, right). We asked whether *et_select*-DNA$_{15}$ might be stable for an alternative lipid loading, testing $\pm$10% and $\pm$20% added lipids relative to the standard APL. In all these cases, the bilayer completely dislodged from the scaffold (Supplementary Figure S10) in at least one of two simulation repeats. Thus, no variation in loading could completely overcome the loss of hydrophobicity and increased negative charge of *et_select*-DNA$_{15}$. We hypothesize that the instability of *et_select*-DNA$_{15}$ scaffolded nanodiscs, which we find *via* simulation, corresponds to the low yield of such nanodiscs *via* experiment;[18] this correspondence, together with the relatively higher *in silico* and *in vitro* stabilities of *dec_select*-DNA$_{15}$ nanodiscs, highlights that our simulations recapitulate the overall experimental trends. However, the fact that at least some nanodiscs based on *et_select*-DNA$_{15}$ could be observed by SEM suggests that there is some aspect of the experiments that our simulations do not capture. For example, we did not model either Mg^{2+} ions or two different lipid types, which were also added to the majority ions and lipids in the experiments. Perhaps the relatively high concentration of Mg^{2+} ions stabilized these nanodiscs by screening scaffold charge; our CG ions do not model the specific and idiosyncratic effects of divalent cations such as Mg^{2+}.[45,46] Overall, our simulations and models highlight the importance of full hydrophobic modification and charge neutralization for scaffolds with shorter hydrophobic moieties such as ethyl groups.

For experimentally reported 15 nm selectively decylated DNA-scaffolded nanodiscs,[18] short-chain (14 carbon) dimyristoyl phosphocholine (DMPC) lipids were used rather than the longer chain (16/18 carbon) POPC lipids we used in most of our simulations. To briefly address this discrepancy with our simulations, we asked simply whether the difference in membrane thickness between selectively decylated and fully ethylated scaffolds would extend to bilayers made of short-chain lipids. CG MARTINI does not have a good model for DMPC, but a good MARTINI model for the even shorter chain DLPC

https://dx.doi.org/10.1021/acsnano.0c07128
ACS Nano XXXX, XXX, XXX−XXX

(12 carbon) was available. Simulations of *dec_select*-DNA_{15}[DLPC] and *et_all*-DNA_{15}[DLPC] scaffolded nanodiscs (Supplementary Figure S11) show that indeed for shorter chain lipids selectively decylated scaffolds still caused significant nanodisc membrane thickening (3.62 nm *vs* 3.46 nm thickness at the peak of the histogram) when compared to fully ethylated scaffolds, which persists noticeably (albeit diminishingly) all the way to the nanodisc center.

45 nm DNA-Scaffolded Nanodiscs. Because our fully ethylated 15 nm scaffold (*et_all*-DNA_{15}) exhibited better bilayer properties than our fully ethylated 11 nm scaffold (*et_all*-DNA_{11}), we explored still larger fully ethylated scaffolds, starting with a fully ethylated dsDNA scaffold *et_all*-DNA_{45}, analogous to the smaller fully ethylated scaffolds. At the end of a 1 μs simulation of *et_all*-DNA_{45} filled with POPC lipids, we observed significant bilayer curvature (Supplementary Figure S12), which conformed to the path traced by the dsDNA scaffold. Membrane curvature can mediate fascinating interactions with guest proteins, which can be sorted to different bilayers[47,48] *via* domains that sense membrane curvature;[49] DNA scaffolds of programmed curvature[22] could be simulated, with guest proteins, to better understand such effects.

Here, however, we are most interested in scaffolds that can create flat, bulk-like bilayers and so—inspired by experiments that show increased bending stiffness for hexagonal bundles of dsDNA[50]—we modeled a 45 nm six-helix bundle ring of hexagonal cross section, with a fully ethylated inner belt (*et_all*-$hexDNA_{45}$, Figure 6A). Within a standard MARTINI CG model for a DNA helix, an intrahelical elastic bond model implements the standard stiffness of the double helix. Within our model, an additional interhelical elastic bond network represents the DNA crossovers, which would constrain the helices in an experimental six-helix bundle. This model closely resembles experimentally produced, liposome-capturing, six-helix bundle rings[21] that were folded using the technique of DNA origami[51] and thus should be experimentally feasible to construct. We chose the inner diameter based on a similarly sized, experimentally validated,[19] hybrid DNA−protein scaffold (explained further below), and only backbone phosphates on the innermost double helix were modified (Figure 1C).

The whole *et_all*-$hexDNA_{45}$ complex, filled with POPC lipids, was simulated for 1 μs. At the end of the simulation the bilayer hosted by *et_all*-$hexDNA_{45}$ had features similar to previous fully ethylated designs, with its thickness small at the edges, rising to and slightly overshooting the thickness of the bulk bilayer (Figure 7A, bottom). Within a 33 nm diameter central region, membrane thickness (ranging from 3.5 to 4 nm around the histogram peak at ∼3.8 nm) was very close to bulk (3.8 nm), and the order parameter (0.33) was, unusually for our simulations, consistently below that of the bulk (0.37). Thus, unlike the smaller nanodiscs, the majority of the membrane area (about 60%) is available to provide guest proteins a native-like membrane thickness and a slightly depressed order parameter.

45 nm Hybrid DNA−Protein Nanodiscs. So far, no large DNA nanorings have been lipidated to yield flat bilayers; only templated liposomes have been achieved with such structures.[21] The reasons for this are yet unclear: it may be that an appropriate scaffold has yet to be tried, an appropriate synthetic protocol simply needs to be found, or both. In the meantime, *ca.* 45 nm nanodiscs have been reported experimentally using hybrid DNA/protein scaffolds,[19] which we model and study here. Briefly, small 11 nm protein nanodiscs with a DNA linker were coupled to large DNA origami corrals (60 or 90 nm outer diameter) along the inner circumference. Large-diameter nanodiscs were then obtained by adding detergent/excess lipid mixture to the DNA corral−protein nanodiscs complexes, which destabilized the small protein nanodiscs. Next, as the detergent was dialyzed out, neighboring protein nanodiscs fused together and grew using the excess lipids. In the end a single large bilayer remained, encircled and stabilized by a number of protein scaffolds that centered the bilayer within the DNA corral *via* DNA linkers.

An ideal model of the hybrid nanodiscs would take into account the complex assembly process that makes them; however the large size of the hybrid nanodiscs makes it difficult to simulate the fusion process. Further, our MD simulation boxes deal with a constant number of particles, and so modeling the detergent removal during dialysis is not possible in a single simulation; the best attempts at modeling changing detergent concentrations resort to performing independent simulations at different lipid:detergent ratios.[52] We avoided such complexity and directly modeled an outer DNA ring (a six-helix bundle equivalent to a DNA origami corral) linked to an inner protein ring: four copies of the linearized protein double-belt scaffold NW_{11} (for a total of eight proteins) arranged into a *ca.* 41 nm diameter ring (Supplementary Figure S1). The protein ring was filled with POPC lipids and coupled to the DNA six-helix bundle *via* four harmonic bond potentials (hexDNA::NW_{11}, where "::" represents the four harmonic bonds; Figure 6B) instead of DNA linkers, under the assumption that this choice would have little effect on membrane properties. The whole complex, 4.2 million particles, was simulated for 1 μs. We observed the usual behavior at membrane edges (Figure 7AB, bottom). Within a 29 nm diameter central region, membrane thickness (∼4 nm) was slightly above the bulk, and the order parameter was almost the same as that found for the bulk bilayer (0.37). Again, unlike the smaller nanodiscs, the majority of the membrane area (about 56%) is available to provide guest proteins a slightly elevated membrane thickness and a native-like order parameter. With respect to which has better membrane properties, large DNA-scaffolded discs or hybrid nanodiscs, we feel that the differences between them are insignificant and potentially artifactual. The area enclosed by the scaffolds changes slightly during simulation, as does lipid wetting of the scaffold, both of which change effective lipid loading and could have some effect on membrane properties. More important is the principle that to achieve a significant area of bulk-like bilayer, much larger nanodiscs should be used.

In experiments with hybrid nanodiscs,[19] binding of a virus to guest protein receptors in the membrane often appeared to cause the protein-scaffolded membrane to break free from the DNA scaffold and tilt out of plane, as visualized in negative stain TEM (see inset in Figure 6C). The authors suggest this is due to a change in membrane tension upon viral binding; we think it is equally plausible that high capillary forces during sample preparation are simply breaking these 3D structures (where 2D nanodiscs without viruses lying flat on the surface are subject to lower capillary forces and experience no disruption). Nevertheless, we were interested in the potential change to membrane properties when the nanodisc is partially freed from the scaffold. Thus, from a configuration at the 0.5 μs time step of a hexDNA::NW_{11} MD trajectory, we deliberately removed two harmonic bonds to create hexDNA:NW_{11} (where ":" represents two harmonic bonds), mimicking a situation in which the protein-scaffolded nanodisc lipid patch is held by only two linkers (Figure 6C). We then simulated hexDNA:NW_{11} for

https://dx.doi.org/10.1021/acsnano.0c07128
ACS Nano XXXX, XXX, XXX−XXX

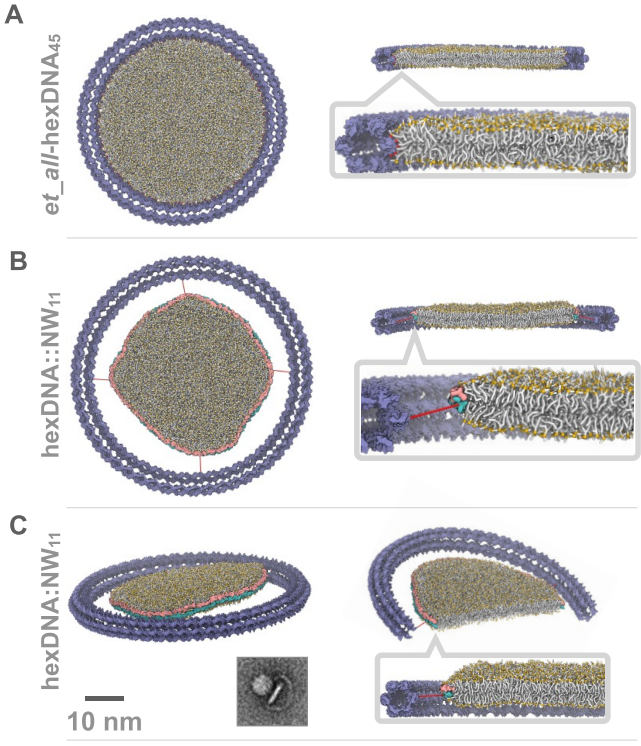

Figure 6. Simulation of 45 nm nanodiscs with POPC bilayers. Top views and cross sections of final configurations (at 1 μs) for (A) a fully ethylated rigid six-helix ring, *et_all*-hexDNA$_{45}$, (B) a six-helix ring with four linkers to a protein nanodisc, hexDNA::NW$_{11}$, and (C) a six-helix ring with two of four linkers, hexDNA:NW$_{11}$. Zoomed cross sections show lipid interactions. In C the inner protein scaffolded disc can dislocate and rotate out of the plane of the DNA ring. Experimental studies have shown that interaction with a viral particle can cause the bilayer plane to tilt steeply relative to the DNA ring (inset adapted with permission from Zhao *et al.*[19] Copyright 2018 ACS *J. Am. Chem. Soc.*). Gray 10 nm scale bars are for full views (not the inset). See Supplementary Figure S3 for number density distribution of lipid head groups around the DNA backbone in the *et_all*-hexDNA$_{45}$ case. Color scheme as in Figure 2 with the addition that harmonic linker bonds are red lines in B and C.

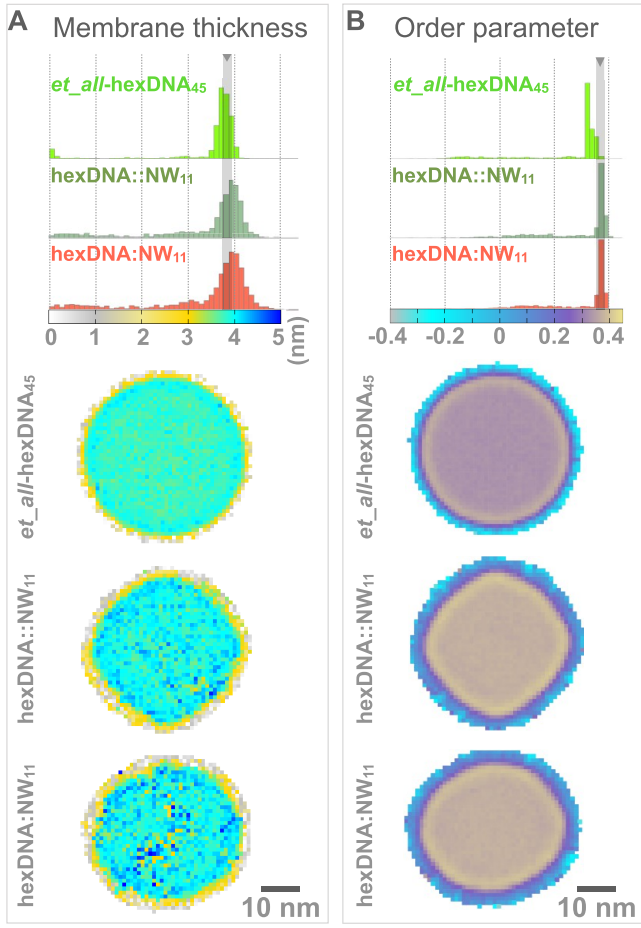

Figure 7. Lipid properties of *ca.* 45 nm POPC-filled nanodiscs. (A) Bilayer thickness and (B) lipid order parameter calculated and plotted for *et_all*-hexDNA$_{45}$ (fully ethylated), hexDNA::NW$_{11}$, and hexDNA:NW$_{11}$ nanodiscs as in Figure 3 (except grid size was 1 × 1 nm^2 for both thickness and order parameter calculations). Normalized histogram distributions are presented at the top; heat map grid plots are presented at the bottom. Extra noise in the membrane thickness for hexDNA::NW$_{11}$ and especially hexDNA:NW$_{11}$, observed as bright yellow and bright blue pixels, is attributed to some fluctuations in membrane curvature in these particular nanodiscs, potentially due to the flexibility of the protein scaffold.

another 0.5 μs. The protein-scaffolded bilayer remained stable but rotated out of the plane of the DNA six-helix bundle. Nonetheless, both the membrane thickness and order parameter (Figure 7) remained similar to those of hexDNA::NW$_{11}$, suggesting that while the outer DNA scaffold is necessary for the formation of the inner protein scaffold, the constraints it imposes are not necessary for maintenance of membrane properties.

Membrane Stability of 11 nm Nanodiscs. In order to form and persist, nanodisc scaffolds must be able to stably bind a lipid bilayer; further, the yield of nanodisc formation may depend on bilayer stability within the scaffold. Where CG MD predicts that nanodiscs created from different scaffolds are all stable over the time scale of simulation, it is of interest to determine which scaffold type creates a more stable nanodisc *via* other means; thus for CG MD-stable nanodiscs, we employed SMD to estimate the force required to dislodge a scaffold from a bilayer patch (Supplementary Methods, SMD Simulations). Similar SMD techniques have been used to calculate the maximum force required to insert carbon nanotubes into lipid bilayers, and calculated forces were found to be of the same order of magnitude as those observed experimentally.[53] This suggests that the type of SMD we employ may be useful as a qualitative guide to experiment.

Given the high computational costs, we limited our SMD studies to small 11 nm nanodiscs. We estimated the maximum force required to dislodge the scaffold from the lipid bilayer patch for protein scaffolded circNW$_{11}$, selectively decylated *dec_select*-DNA$_{11}$, and fully ethylated *et_all*-DNA$_{11}$ nanodiscs (Figure 8). We took an approach similar to one that we have used previously,[39] in which SMD was used to study the force required to pull ethyl-modified DNA nanopore modifications out of lipid bilayers. Here, we pulled the center of mass (COM) of scaffold backbone beads (protein or DNA) away from the COM of lipid phosphate head groups at a constant rate of 10 nm μs^{-1}. From four different starting configurations, we performed four independent 1 μs SMD simulations, for each scaffold type. To prevent lipids from being pulled along with the scaffolds, we applied weak positional restraints to the lipid phosphate head groups. Lipid tails were left free to interact with the scaffolds without any restraints. In all cases, the peak (maximum) force

https://dx.doi.org/10.1021/acsnano.0c07128
ACS Nano XXXX, XXX, XXX−XXX

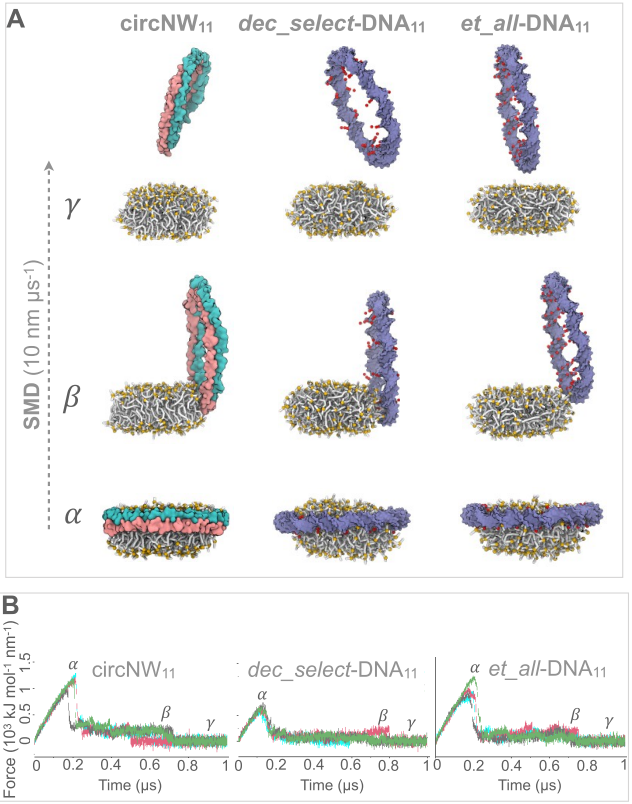

Figure 8. Dislodging scaffolds from nanodiscs. (A) Snapshots of SMD simulations for three different scaffolds (protein SMD-circNW$_{11}$, selectively decylated SMD-*dec_select*-DNA$_{11}$, and fully ethylated SMD-*et_all*-DNA$_{11}$). The center of mass of the scaffold is pulled away at a constant rate (10 nm μs^{-1}) from the center of mass of the lipid bilayer patch. α, β, and γ snapshots correspond to the labels shown in SMD force profiles in B. For representative initial configurations at t = 0 see Figure 2. For each case, α shows when most of the scaffold is first off-center from the lipid bilayer, β shows when most of the scaffold dislodged, with few lipid interactions, and finally γ shows when the scaffold is fully detached from the lipid patch. (B) Pulling-force profiles. In each case four different SMDs (gray, cyan, red, green) were performed starting from different pre-equilibrated configurations; thus peak forces vary slightly between repeats.

(Figure 8A and B, "α" stage) required to dislodge the scaffold from the center of bilayer patch while still remaining in contact with the lipids was observed at early times. At later times, no significant change in force was observed, because most of the scaffold had been dislodged (Figure 8A, "β" stage). We continued the SMD until there was no interaction (average pull force was 0, Figure 8A "γ" stage) between the scaffold and the lipids.

The peak force was highest (1204 ± 91 kJ mol^{-1} nm^{-1}, 2000 pN) for protein scaffold SMD-circNW$_{11}$. For the fully ethylated DNA scaffold (SMD-*et_all*-DNA$_{11}$) the maximum force was slightly lower, 1075 ± 118 kJ mol^{-1} nm^{-1} (1786 pN, Figure 8B), 89% of the peak force for the protein scaffold. The peak force for the selectively decylated DNA scaffold (SMD-*dec_select*-DNA$_{11}$) was the lowest, at 687 ± 57 kJ mol^{-1} nm^{-1} (1141 pN, Figure 8B), only 57% of that observed for SMD-circNW$_{11}$. Here, SMD confirms the instability of *dec_select*-DNA$_{11}$ which was hinted at by tilting of the scaffold in CG MD. We attribute this instability to unfavorable interactions of lipids with the exposed negatively charged DNA phosphate backbone of the *dec_select*-DNA$_{11}$ scaffold. This result is consistent with our previous studies[39] on DNA nanopore interaction with lipid membranes, where we observed a drop in maximum force profiles for nanopores in which negatively charged DNA backbone sites were exposed to the lipids.

To control for lipid loading, we performed additional SMD simulations (Supplementary Figure S13) for selected 11 nm DNA-scaffolded nanodiscs containing ±10% lipid, relative to the standard APL. For 10% less lipids, the peak force required to dislodge a scaffold decreased for both $^{-10\%}$*et_all*-DNA11 (1002 ± 49 kJ mol^{-1} nm^{-1}, 1664 pN, −7%) and $^{-10\%}$*dec_select*-DNA$_{11}$ (615 ± 108 kJ mol^{-1} nm^{-1}, 1021 pN, −10%), but the relationship between peak forces for fully ethylated and selectively decylated scaffolds remained roughly the same (~60% higher for fully ethylated). In contrast, using 10% more lipids resulted in an increase in peak force for $^{+10\%}$*et_all*-DNA$_{11}$ (1238 ± 23 kJ mol^{-1} nm^{-1}, 2056 pN, +15%); we did not attempt to measure a peak force for $^{+10\%}$*dec_select*-DNA$_{11}$, as we had already found it unstable in CG MD above.

Overall, our simulations support the idea that SMD may be able to resolve differences between nanodiscs whose stability is otherwise difficult to distinguish by CG MD. It remains an interesting and open question whether peak forces for scaffold dislocation could be used to predict the yield of experimentally synthesized nanodiscs or whether differences in peak forces measured for different lipid loading could translate into differences in yield for syntheses having different lipid:scaffold stoichiometries or even a distribution of nanodiscs having different APL within a single experiment. If yields or distributions of nanodiscs having different lipid loading could be accurately measured, then it is possible that the combination of SMD with the Jarzinski equality could quantitatively predict these yields or distributions.[54−56]

CONCLUSIONS

Lipid bilayer properties can have important implications for the structure and function of the membrane proteins, *e.g.*, bilayer thickness affects gating properties[57] and folding pathways[58] of membrane proteins. For nanodiscs, bilayer properties depend intimately on details of the scaffold. Here, we have employed CG MD and SMD to determine what sizes and types of nanodisc scaffolds best support a stable lipid bilayer with lipid properties comparable to bulk membranes. A number of principles for nanodisc scaffold design can be drawn from our simulation results.

In all our simulations, lipids close to the scaffold had properties very different from those in the bulk bilayer. Independent of scaffold type, 11 nm scaffolds had the most perturbed properties, never achieving bulk bilayer properties even in the center of the disc. However, in fully ethylated 15 nm DNA scaffolds, which had a completely neutral hydrophobic inner belt, we found that bulk bilayer membrane properties were achieved a few nanometers from the scaffold's edge. Our results show that increasing the nanodisc size, from 11 nm to 15 nm using a fully ethylated scaffold, improves bilayer properties. This contrasts the case of selectively decylated scaffolds, for which lipid properties did not improve with an increase in nanodisc size. Thus, the scaffold size alone does not improve the membrane properties, but the scaffold type also plays an important role. For smaller membrane proteins or membrane protein complexes, we suggest that 15 nm DNA scaffolds with fully ethylated residues may enable proteins to achieve native-like function. For larger guest proteins or larger complexes,

https://dx.doi.org/10.1021/acsnano.0c07128
ACS Nano XXXX, XXX, XXX−XXX

requiring 45 nm nanodiscs, fully ethylated single-helix scaffolds may prove too floppy, as our simulations indicate that they can have significant curvature. However, we observe that 45 nm nanodiscs constructed from six-helix bundles are both rigid and possess bulk-like properties over the majority of their area. In general, laboratory experiments use the smallest nanodiscs that accommodate the protein of interest (for the understandable reasons of cost and complexity). However, because lipids close to the scaffold deviate strongly from bulk membrane behavior, we suggest that "oversizing" a nanodisc relative to the intended guest protein by at least a few nanometers will give the highest probability of achieving native-like protein behavior. Examining the potential importance of this heuristic with simulated and real guest proteins is an important goal for both future MD and laboratory experiments.

Larger nanodisc scaffolds are synthetically expensive, but they have other potentially useful properties besides simply achieving bulk-like behavior. DNA origami scaffolds are particularly suited for arranging different numbers and types of proteins within a membrane to study their protein−protein interactions. This can be achieved because the hundreds of short "staple strands" that comprise origami are easily modified with unique linkers that serve as addressable spots for membrane protein attachment and subsequent release into the bilayer. Although still hypothetical, here DNA-only scaffolds have potential advantages over DNA−protein hybrid scaffolds. In addition to the synthetic complexity and apparent fragility of the hybrid scaffolds (as shown in the case of viral interactions), hybrid scaffolds have a large and variable gap between the outer DNA ring and the edge of the bilayer, which will require longer linkers for membrane proteins tethered to the DNA ring, decreasing control and potentially yield of desired protein arrangements. One programmable platform for the study of membrane proteins has already been demonstrated with DNA origami supported liposomes;[59] the achievement of pure DNA origami nanodisc scaffolds will require both the right design (in terms of hydrophobic modification type and arrangement) and an appropriate experimental lipidation protocol.

It is often thought that hydrophobic DNA modifications that are more lipid-like, or longer, give better bilayer binding properties or more stable DNA−lipid constructs without regard to other variables. Scaffolds from the experimental study[18] that we reproduce here in simulation have been cited as evidence for this,[60] with decyl being quoted as giving higher yields than ethyl groups. For a fixed charge density, longer hydrophobic modifications will likely increase construct stability, but the reported[18] scaffolds are not evidence for this, as ethylated scaffolds had half the modification density of decylated scaffolds and were thus incomparable. Our current study should motivate scaffold designers to deemphasize modification size *per se* and think more in terms of total hydrophobic content and remnant charge density on a modified scaffold. Our main evidence is that for two scaffold sizes, ethylated scaffolds with lower total hydrophobic content than comparable decylated scaffolds (15% lower for 11 nm and 8% lower for 15 nm), CG MD bilayer properties were significantly better, and for 11 nm discs, SMD bilayer stability was significantly higher. Furthermore, bilayer properties for 11 nm fully ethylated DNA-scaffolded nanodiscs were even better than that of equivalently sized protein nanodiscs. Based on previously believed heuristics (*e.g.*, longer hydrophobic modifications yield better lipid binding), the fully ethylated scaffolds should have performed worse than the selectively decylated scaffolds, and yet full charge neutralization resulted in better performance. In general, with respect to synthesizability and handling, an increased total hydrophobic content tends to decrease yield, decrease solubility, and increase aggregation. Thus, for a fixed budget of total hydrophobic content, we propose that scaffold designers are better off using many smaller, less lipid-like modifications, which provide better charge neutralization. For a fixed hydrophobic content, increased charge neutralization of DNA scaffolds may itself come at the cost of more difficult handling, but this must be better explored.

When drawing conclusions from Martini CG models, one should keep their limitations in mind.[61] For example, Martini DNA models currently use an extensive elastic bond network to keep the double-helical structure intact. This adds some rigidity to the models, which may or may not alter their interactions with lipids. Though computationally expensive, all-atom MD is more precise and can simultaneously capture a wider variety of phenomena than can CG MD. For example, Yoo and Aksimentiev[62] used all-atom MD to simultaneously study ion conductance through a lipid membrane spanning DNA channel and observe DNA structural fluctuations. Hybrid CG and all-atom approaches can provide the best of both worlds: CG MD can be run quickly to equilibrium, and the resulting configurations can provide starting points for much slower but more accurate all-atom simulations. As we have previously used for DNA nanopores,[39] such hybrid approaches could be applied to our nanodisc models, so that DNA, lipid, and ion interactions could be captured more precisely, all at once.

Our work provides insights that may help design and construct nanodiscs that are both stable and behave similarly to bulk bilayers. While these properties may be necessary to achieve native protein behavior in nanodiscs, they may not be sufficient. Thus, an important avenue for future work is to simulate systems in which guest proteins are placed within nanodiscs of various sizes, filled with mixtures of lipids having compositions more similar to those found in biological membranes. Further, with the goal of creating the best possible membrane model in mind, we observe that natural biological membranes are highly asymmetric, with respect to both protein orientation and lipid composition between the two leaflets of a bilayer; control of such asymmetries in nanodiscs has yet to be achieved. DNA scaffolds, in particular, offer an exciting opportunity to control and study the effects of such asymmetries: tether length (*e.g.*, a DNA linker) and scaffold geometry should be able to control protein orientation, and the distribution of hydrophobic modification types (*e.g.*, adding cholesterols on one face of a DNA ring and ethyls on the other or strategically leaving some inward-facing DNA phosphates charged) should affect the equilibrium distribution of lipid types between the bilayer leaflets. The dynamics of lipid exchange will also be accessible: DNA-catalyzed flipping of lipids from one leaflet to another has been observed *via* MD, and this phenomena has been exploited to create DNA enzymes that catalyze lipid flipping in liposomes in the lab.[63,64] Should such DNA flippases prove insufficient, others have proposed[65] the use of tethered protein flippases or methyl-β-cyclodextrins[66] to create bilayer asymmetry. Looking forward, we anticipate that CG MD of symmetry-broken nanodiscs will play an important role in our understanding of asymmetric lipid bilayers.

METHODS

Modeling. First we built all-atom DNA ring scaffolds using Nucleic Acid Builder,[67] and the all-atom protein scaffold (cNW11) was

https://dx.doi.org/10.1021/acsnano.0c07128
ACS Nano XXXX, XXX, XXX−XXX

obtained from CHARMM-GUI builder.[31] From all-atom models, we generated CG models using *martinize.py*[68] for proteins and stiff *martinize-dna.py*[69] for dsDNA. Further hydrophobic modifications on DNA scaffolds were done using our own custom PERL scripts. Details, including CG circNW$_{11}$ and CG DNA−protein hybrid scaffold model building, are described in the Supplementary Methods.

MD Simulations. In most cases POPC lipids, in the form of a bilayer lattice, were inserted inside the scaffold rings using the *insane.py*[43] script. For two cases, *dec_select*-DNA$_{15}$[DLPC] and *et_all*-DNA$_{15}$[DLPC], we inserted DLPC lipids (MARTINI's closest equivalent to DMPC lipids). The hydrophobic belt of the scaffold ring was centered along the acyl lipid tails. Lipids outside the ring were removed using our own PERL scripts, and the number of lipids within the ring was calculated based on the surface area of the ring (innermost diameter) and the area per lipid (APL). For POPC we used an APL of 0.683 nm^2 and for DLPC we used 0.641 nm^2; these are the same values used by CHARMM-GUI builder.[31] For the pure POPC bulk bilayer, we generated the initial membrane configuration (20 × 20 nm^2 patch) using *insane.py*.[43] For 11 nm scaffolds, the internal diameters are almost the same, which thus allowed us to keep the number of lipids per nanodisc constant. We also did this for unbiased SMD force profile calculations; that is, the "hydrophobic content" of the lipid patch remains the same, but different types of scaffolds are pulled away. In all cases, CG water particles and CG Na^+ and Cl^- ions (at a concentration of 0.15 M) were added using utilities in GROMACS v2019.4.[70,71] Depending on nanodisc size, the final dimensions of the simulation boxes were as follows: *ca.* 16 × 16 × 16 nm^3 in 11 nm nanodiscs, *ca.* 20 × 20 × 20 nm^3 in 15 nm nanodiscs, *ca.* 65 × 65 × 65 nm^3 for *et_all*-DNA$_{45}$, *ca.* 74 × 74 × 74 nm^3 for *et_all*-hexDNA$_{45}$, and *ca.* 80 × 80 × 80 nm^3 for hexDNA:NW$_{11}$ and hexDNA::NW$_{11}$. The box size for the POPC bulk bilayer was *ca.* 20 × 20 × 10 nm^3.

CG simulations based on MARTINI DNA,[69] protein,[68] and lipid[43] force fields were run on GPUs using GROMACS v2019.4[70,71] (www.gromacs.org). Starting configurations were subjected to steepest-descent energy minimization to remove close contacts. After this, in the *et_all*-hexDNA$_{45}$ case for 100 ps, with a small time step of 1 fs, we applied position restraints with force constant of 10^4 kJ mol^{-1} nm^{-2} to DNA and lipid phosphate head groups. In hexDNA::NW$_{11}$, positional restraints on the protein backbone and lipid head groups were removed slowly from 1000, 500, 250, 100, and 10 kJ mol^{-1} nm^{-2} over 25 ns (each positional restraint applied for 5 ns). Later, in all the cases, the system was equilibrated for 10 ns with a 20 fs time step without any position restraints. The Berendsen barostat[72] with a coupling constant of 3 ps was used to control isotropic pressure at 1 bar for the nanodiscs. For pure POPC bulk bilayers, semi-isotropic pressure control was used. A temperature of 300 K was maintained using a velocity rescale thermostat[73] with a 2 ps coupling constant. For different repeats of MD simulations, random seeds were provided at this step for generating velocities. We used the standard set of parameters recommended with the MARTINI force field.[74] The cutoff for van der Waals and Coulombic interactions was set to 1.1 nm and with the potential-modifier implemented in GROMACS it was shifted to zero. After every 10 steps, the Verlet[75] neighbor list was updated. Final production runs were simulated up to 1 μs. For nanodisc production runs, an isotropic pressure of 1 bar was maintained using a Parrinello−Rahman barostat[76] with a 12 ps coupling constant and a velocity rescale thermostat[73] with a 1 ps coupling constant used for maintaining the temperature at 300 K. The rest of the parameters remained the same, and semi-isotropic pressure control was used for pure POPC bilayer production runs.

For hexDNA:NW$_{11}$ (with only two harmonic connections with the DNA scaffold) we obtained the initial configuration from the production run of hexDNA::NW$_{11}$ at the 0.5 μs time step. Then, keeping only two harmonic bonds out of the four in hexDNA::NW$_{11}$, at the opposite ends, the system was run further for 0.5 μs using production run parameters described above.

Additional SMD simulation details are provided in the Supplementary Methods.

Analyses. In-house PERL scripts and GROMACS v2019.4 utilities were used for the analyses. Plots were created using *gnuplot* (www.gnuplot.info) and *matplotlib*.[77] Snapshot images were rendered with VMD.[78] Analyses were performed on the last 0.4 μs of the equilibrated trajectory, sampled every 100 ps, and averaged over the repeats. Membrane thickness and order parameter calculations are described in Supplementary Methods.

ASSOCIATED CONTENT

Supporting Information

The Supporting Information is available free of charge at https://pubs.acs.org/doi/10.1021/acsnano.0c07128.

DNA, protein, and hybrid DNA−protein scaffold model building; description of membrane thickness and order parameter analyses; SMD simulation details; additional supporting figures (PDF)

Movie S1: Last 20 ns of simulation for circNW$_{11}$ from Figure 2A (MPG)

Movie S2: Last 20 ns of simulation for dec_select-DNA$_{11}$ from Figure 2B (MPG)

Movie S3: Last 20 ns of simulation for et_all-DNA$_{11}$ from Figure 2C (MPG)

Movie S4: Last 20 ns of simulation for dec_select-DNA$_{15}$ from Figure 4A (MPG)

Movie S5: Last 20 ns of simulation for et_all-DNA$_{15}$ from Figure 4B (MPG)

Movie S6: Last 10 ns of simulation for et_all-hexDNA$_{45}$ from Figure 6A (MPG)

Movie S7: Last 10 ns of simulation for hexDNA::NW$_{11}$ from Figure 6B (MPG)

AUTHOR INFORMATION

Corresponding Authors

Vishal Maingi − *Department of Bioengineering, California Institute of Technology, Pasadena, California 91125, United States;* orcid.org/0000-0003-3861-7973; Email: vmaingi@caltech.edu, maingivishal@gmail.com

Paul W. K. Rothemund − *Departments of Bioengineering, Computing + Mathematical Sciences, and Computation & Neural Systems, California Institute of Technology, Pasadena, California 91125, United States;* orcid.org/0000-0002-1653-3202; Email: pwkr@dna.caltech.edu

Complete contact information is available at: https://pubs.acs.org/10.1021/acsnano.0c07128

Author Contributions

V.M. designed the computational studies, and performed and analysed all simulations. V.M. and P.W.K.R. discussed and wrote the manuscript.

Notes

The authors declare no competing financial interest.

ACKNOWLEDGMENTS

V.M. thanks Mark S. P. Sansom for initial talks concerning small-sized nanodiscs, which seeded the motivation for this study, and Helgi Ingólfsson for MARTINI force field discussions. V.M. acknowledges a Human Frontier Science Program Postdoctoral fellowship and cloud computation credits from Amazon Web Services-Caltech program. P.W.K.R. acknowledges the National Science Foundation (1636364) and the Office of Naval Research (N00014-18-12649 and N00014-17-12610).

REFERENCES

(1) Engel, A.; Gaub, H. E. Structure and Mechanics of Membrane Proteins. *Annu. Rev. Biochem.* **2008**, *77*, 127−148.

https://dx.doi.org/10.1021/acsnano.0c07128
ACS Nano XXXX, XXX, XXX−XXX

(2) Denisov, I. G.; Sligar, S. G. Nanodiscs in Membrane Biochemistry and Biophysics. *Chem. Rev.* **2017**, *117*, 4669−4713.
(3) Nasr, M. L. Large Nanodiscs Going Viral. *Curr. Opin. Struct. Biol.* **2020**, *60*, 150−156.
(4) Andersen, O. S.; Koeppe, R. E. Bilayer Thickness and Membrane Protein Function: An Energetic Perspective. *Annu. Rev. Biophys. Biomol. Struct.* **2007**, *36*, 107−130.
(5) Dumas, F.; Tocanne, J.-F.; Leblanc, G.; Lebrun, M.-C. Consequences of Hydrophobic Mismatch between Lipids and Melibiose Permease on Melibiose Transport. *Biochemistry* **2000**, *39*, 4846−4854.
(6) Martens, C.; Stein, R. A.; Masureel, M.; Roth, A.; Mishra, S.; Dawaliby, R.; Konijnenberg, A.; Sobott, F.; Govaerts, C.; Mchaourab, H. S. Lipids Modulate the Conformational Dynamics of a Secondary Multidrug Transporter. *Nat. Struct. Mol. Biol.* **2016**, *23*, 744−751.
(7) Wang, Q.; Corey, R. A.; Hedger, G.; Aryal, P.; Grieben, M.; Nasrallah, C.; Baronina, A.; Pike, A. C. W.; Shi, J.; Carpenter, E. P.; Sansom, M. S. P. Lipid Interactions of a Ciliary Membrane TRP Channel: Simulation and Structural Studies of Polycystin-2. *Structure* **2019**, *28*, 169−184.
(8) Cao, E.; Cordero-Morales, J. F.; Liu, B.; Qin, F.; Julius, D. TRPV1 Channels Are Intrinsically Heat Sensitive and Negatively Regulated by Phosphoinositide Lipids. *Neuron* **2013**, *77*, 667−679.
(9) Bibow, S. Exploring Lipid and Membrane Protein Dynamics Using Lipid-Bilayer Nanodiscs and Solution-State NMR Spectroscopy. In *Expression, Purification, and Structural Biology of Membrane Proteins*, 1st ed.; Perez, C., Maier, T., Eds.; Methods in Molecular Biology; Springer US: New York, NY, 2020; Vol. *2127*, pp 397−419.
(10) Sackmann, E. Physical Basis of Self-Organization and Function of Membranes: Physics of Vesicles. In *Structure and Dynamics of Membranes*, 1st ed.; Lipowsky, R., Sackmann, E., Eds.; Handbook of Biological Physics; Elsevier Science: North-Holland, 1995; Vol. *1*, pp 213−304.
(11) Piggot, T. J.; Allison, J. R.; Sessions, R. B.; Essex, J. W. On the Calculation of Acyl Chain Order Parameters from Lipid Simulations. *J. Chem. Theory Comput.* **2017**, *13*, 5683−5696.
(12) Marrink, S. J.; de Vries, A. H.; Mark, A. E. Coarse Grained Model for Semiquantitative Lipid Simulations. *J. Phys. Chem. B* **2004**, *108*, 750−760.
(13) Mitchell, D. C.; Straume, M.; Miller, J. L.; Litman, B. J. Modulation of Metarhodopsin Formation by Cholesterol-Induced Ordering of Bilayer Lipids. *Biochemistry* **1990**, *29*, 9143−9149.
(14) Bayburt, T. H.; Grinkova, Y. V.; Sligar, S. G. Self-Assembly of Discoidal Phospholipid Bilayer Nanoparticles with Membrane Scaffold Proteins. *Nano Lett.* **2002**, *2*, 853−856.
(15) Pourmousa, M.; Pastor, R. W. Molecular Dynamics Simulations of Lipid Nanodiscs. *Biochim. Biophys. Acta, Biomembr.* **2018**, *1860*, 2094−2107.
(16) Nasr, M. L.; Baptista, D.; Strauss, M.; Sun, Z.-Y. J.; Grigoriu, S.; Huser, S.; Plückthun, A.; Hagn, F.; Walz, T.; Hogle, J. M.; Wagner, G. Covalently Circularized Nanodiscs for Studying Membrane Proteins and Viral Entry. *Nat. Methods* **2017**, *14*, 49−52.
(17) Knowles, T. J.; Finka, R.; Smith, C.; Lin, Y.-P.; Dafforn, T.; Overduin, M. Membrane Proteins Solubilized Intact in Lipid Containing Nanoparticles Bounded by Styrene Maleic Acid Copolymer. *J. Am. Chem. Soc.* **2009**, *131*, 7484−7485.
(18) Iric, K.; Subramanian, M.; Oertel, J.; Agarwal, N. P.; Matthies, M.; Periole, X.; Sakmar, T. P.; Huber, T.; Fahmy, K.; Schmidt, T. L. DNA-Encircled Lipid Bilayers. *Nanoscale* **2018**, *10*, 18463−18467.
(19) Zhao, Z.; Zhang, M.; Hogle, J. M.; Shih, W. M.; Wagner, G.; Nasr, M. L. DNA-Corralled Nanodiscs for the Structural and Functional Characterization of Membrane Proteins and Viral Entry. *J. Am. Chem. Soc.* **2018**, *140*, 10639−10643.
(20) Zhang, Z.; Yang, Y.; Pincet, F.; Llaguno, M. C.; Lin, C. Placing and Shaping Liposomes with Reconfigurable DNA Nanocages. *Nat. Chem.* **2017**, *9*, 653−659.
(21) Yang, Y.; Wang, J.; Shigematsu, H.; Xu, W.; Shih, W. M.; Rothman, J. E.; Lin, C. Self-Assembly of Size-Controlled Liposomes on DNA Nanotemplates. *Nat. Chem.* **2016**, *8*, 476.
(22) Franquelim, H. G.; Khmelinskaia, A.; Sobczak, J.-P.; Dietz, H.; Schwille, P. Membrane Sculpting by Curved DNA Origami Scaffolds. *Nat. Commun.* **2018**, *9*, 811.
(23) Zhang, Z.; Chapman, E. R. Programmable Nanodisc Patterning by DNA Origami. *Nano Lett.* **2020**, *20*, 6032−6037.
(24) Hagn, F.; Etzkorn, M.; Raschle, T.; Wagner, G. Optimized Phospholipid Bilayer Nanodiscs Facilitate High-Resolution Structure Determination of Membrane Proteins. *J. Am. Chem. Soc.* **2013**, *135*, 1919−1925.
(25) Burns, J. R.; Stulz, E.; Howorka, S. Self-Assembled DNA Nanopores That Span Lipid Bilayers. *Nano Lett.* **2013**, *13*, 2351−2356.
(26) Langecker, M.; Arnaut, V.; Martin, T. G.; List, J.; Renner, S.; Mayer, M.; Dietz, H.; Simmel, F. C. Synthetic Lipid Membrane Channels Formed by Designed DNA Nanostructures. *Science* **2012**, *338*, 932−936.
(27) Burns, J. R.; Göpfrich, K.; Wood, J. W.; Thacker, V. V.; Stulz, E.; Keyser, U. F.; Howorka, S. Lipid-Bilayer-Spanning DNA Nanopores with a Bifunctional Porphyrin Anchor. *Angew. Chem., Int. Ed.* **2013**, *52*, 12069−12072.
(28) Debnath, A.; Schäfer, L. V. Structure and Dynamics of Phospholipid Nanodiscs from All-Atom and Coarse-Grained Simulations. *J. Phys. Chem. B* **2015**, *119*, 6991−7002.
(29) Pourmousa, M.; Song, H. D.; He, Y.; Heinecke, J. W.; Segrest, J. P.; Pastor, R. W. Tertiary Structure of Apolipoprotein A-I in Nascent High-Density Lipoproteins. *Proc. Natl. Acad. Sci. U. S. A.* **2018**, *115*, 5163LP−5168.
(30) Siuda, I.; Tieleman, D. P. Molecular Models of Nanodiscs. *J. Chem. Theory Comput.* **2015**, *11*, 4923−4932.
(31) Qi, Y.; Lee, J.; Klauda, J. B.; Im, W. CHARMM-GUI Nanodisc Builder for Modeling and Simulation of Various Nanodisc Systems. *J. Comput. Chem.* **2019**, *40*, 893−899.
(32) Schachter, I.; Allolio, C.; Khelashvili, G.; Harries, D. Confinement in Nanodiscs Anisotropically Modifies Lipid Bilayer Elastic Properties. *J. Phys. Chem. B* **2020**, *124*, 7166−7175.
(33) Bengtsen, T.; Holm, V. L; Kjølbye, L. R.; Midtgaard, S. R.; Johansen, N. T.; Tesei, G.; Bottaro, S.; Schiøtt, B.; Arleth, L.; Lindorff-Larsen, K. Structure and Dynamics of a Nanodisc by Integrating NMR, SAXS and SANS Experiments with Molecular Dynamics Simulations. *eLife* **2020**, *9*, No. e56518.
(34) Mei, X.; Atkinson, D. Crystal Structure of C-Terminal Truncated Apolipoprotein A-I Reveals the Assembly of High Density Lipoprotein (HDL) by Dimerization. *J. Biol. Chem.* **2011**, *286*, 38570−38582.
(35) Borhani, D. W.; Rogers, D. P.; Engler, J. A.; Brouillette, C. G. Crystal Structure of Truncated Human Apolipoprotein A-I Suggests a Lipid-BoundConformation. *Proc. Natl. Acad. Sci. U. S. A.* **1997**, *94*, 12291LP−12296.
(36) Bibow, S.; Polyhach, Y.; Eichmann, C.; Chi, C. N.; Kowal, J.; Albiez, S.; McLeod, R. A.; Stahlberg, H.; Jeschke, G.; Güntert, P.; Riek, R. Solution Structure of Discoidal High-Density Lipoprotein Particles with a Shortened Apolipoprotein A-I. *Nat. Struct. Mol. Biol.* **2017**, *24*, 187−193.
(37) Marrink, S. J.; Risselada, H. J.; Yefimov, S.; Tieleman, D. P.; de Vries, A. H. The MARTINI Force Field: Coarse Grained Model for Biomolecular Simulations. *J. Phys. Chem. B* **2007**, *111*, 7812−7824.
(38) Ingólfsson, H. I.; Lopez, C. A.; Uusitalo, J. J.; de Jong, D. H.; Gopal, S. M.; Periole, X.; Marrink, S. J. The Power of Coarse Graining in Biomolecular Simulations. *Wiley Interdiscip. Rev. Comput. Mol. Sci.* **2014**, *4*, 225−248.
(39) Maingi, V.; Burns, J. R.; Uusitalo, J. J.; Howorka, S.; Marrink, S. J.; Sansom, M. S. P. Stability and Dynamics of Membrane-Spanning DNA Nanopores. *Nat. Commun.* **2017**, *8*, 14784.
(40) Maingi, V. *DNA Nanotubes and Their Interaction with Membranes: Insights through Multiscale Molecular Dynamics Simulations*. PhD thesis, University of Oxford, Oxford, UK, 2016.
(41) Kučerka, N.; Nieh, M.-P.; Katsaras, J. Fluid Phase Lipid Areas and Bilayer Thicknesses of Commonly Used Phosphatidylcholines as a Function of Temperature. *Biochim. Biophys. Acta, Biomembr.* **2011**, *1808*, 2761−2771.

https://dx.doi.org/10.1021/acsnano.0c07128
ACS Nano XXXX, XXX, XXX−XXX

(42) Lewis, B. A.; Engelman, D. M. Lipid Bilayer Thickness Varies Linearly with Acyl Chain Length in Fluid Phosphatidylcholine Vesicles. *J. Mol. Biol.* **1983**, *166*, 211−217.
(43) Wassenaar, T. A.; Ingólfsson, H. I.; Böckmann, R. A.; Tieleman, D. P.; Marrink, S. J. Computational Lipidomics with Insane: A Versatile Tool for Generating Custom Membranes for Molecular Simulations. *J. Chem. Theory Comput.* **2015**, *11*, 2144−2155.
(44) Denisov, I. G.; Grinkova, Y. V.; Lazarides, A. A.; Sligar, S. G. Directed Self-Assembly of Monodisperse Phospholipid Bilayer Nanodiscs with Controlled Size. *J. Am. Chem. Soc.* **2004**, *126*, 3477−3487.
(45) Guéroult, M.; Boittin, O.; Mauffret, O.; Etchebest, C.; Hartmann, B. Mg^{2+} in the Major Groove Modulates B-DNA Structure and Dynamics. *PLoS One* **2012**, *7*, No. e41704.
(46) Yu, J.; Ha, T.; Schulten, K. Conformational Model of the Holliday Junction Transition Deduced from Molecular Dynamics Simulations. *Nucleic Acids Res.* **2004**, *32*, 6683−6695.
(47) Moreno-Pescador, G.; Florentsen, C. D.; Østbye, H.; Sønder, S. L.; Boye, T. L.; Veje, E. L.; Sonne, A. K.; Semsey, S.; Nylandsted, J.; Daniels, R.; Bendix, P. M. Curvature- and Phase-Induced Protein Sorting Quantified in Transfected Cell-Derived Giant Vesicles. *ACS Nano* **2019**, *13*, 6689−6701.
(48) Rosholm, K. R.; Leijnse, N.; Mantsiou, A.; Tkach, V.; Pedersen, S. L.; Wirth, V. F.; Oddershede, L. B.; Jensen, K. J.; Martinez, K. L.; Hatzakis, N. S.; Bendix, P. M.; Callan-Jones, A.; Stamou, D. Membrane Curvature Regulates Ligand-Specific Membrane Sorting of GPCRs in Living Cells. *Nat. Chem. Biol.* **2017**, *13*, 724−729.
(49) Zeno, W. F.; Thatte, A. S.; Wang, L.; Snead, W. T.; Lafer, E. M.; Stachowiak, J. C. Molecular Mechanisms of Membrane Curvature Sensing by a Disordered Protein. *J. Am. Chem. Soc.* **2019**, *141*, 10361−10371.
(50) Kauert, D. J.; Kurth, T.; Liedl, T.; Seidel, R. Direct Mechanical Measurements Reveal the Material Properties of Three-Dimensional DNA Origami. *Nano Lett.* **2011**, *11*, 5558−5563.
(51) Rothemund, P. W. K. Folding DNA to Create Nanoscale Shapes and Patterns. *Nature* **2006**, *440*, 297−302.
(52) Shih, A. Y.; Freddolino, P. L.; Sligar, S. G.; Schulten, K. Disassembly of Nanodiscs with Cholate. *Nano Lett.* **2007**, *7*, 1692−1696.
(53) Wallace, E. J.; Sansom, M. S. P. Blocking of Carbon Nanotube Based Nanoinjectors by Lipids: A Simulation Study. *Nano Lett.* **2008**, *8*, 2751−2756.
(54) Park, S.; Khalili-Araghi, F.; Tajkhorshid, E.; Schulten, K. Free Energy Calculation from Steered Molecular Dynamics Simulations Using Jarzynski's Equality. *J. Chem. Phys.* **2003**, *119*, 3559−3566.
(55) Boubeta, F. M.; Contestín García, R. M.; Lorenzo, E. N.; Boechi, L.; Estrin, D.; Sued, M.; Arrar, M. Lessons Learned about Steered Molecular Dynamics Simulations and Free Energy Calculations. *Chem. Biol. Drug Des.* **2019**, *93*, 1129−1138.
(56) Ho, K.; Truong, D. T.; Li, M. S. How Good Is Jarzynski's Equality for Computer-Aided Drug Design? *J. Phys. Chem. B* **2020**, *124*, 5338−5349.
(57) Rostovtseva, T. K.; Kazemi, N.; Weinrich, M.; Bezrukov, S. M. Voltage Gating of VDAC Is Regulated by Nonlamellar Lipids of Mitochondrial Membranes. *J. Biol. Chem.* **2006**, *281*, 37496−37506.
(58) Hong, H.; Tamm, L. K. Elastic Coupling of Integral Membrane Protein Stability to Lipid Bilayer Forces. *Proc. Natl. Acad. Sci. U. S. A.* **2004**, *101*, 4065LP−4070.
(59) Xu, W.; Nathwani, B.; Lin, C.; Wang, J.; Karatekin, E.; Pincet, F.; Shih, W.; Rothman, J. E. A Programmable DNA Origami Platform to Organize SNAREs for Membrane Fusion. *J. Am. Chem. Soc.* **2016**, *138*, 4439−4447.
(60) Darley, E.; Singh, J. K. D.; Surace, N. A.; Wickham, S. F. J.; Baker, M. A. B. The Fusion of Lipid and DNA Nanotechnology. *Genes* **2019**, *10*, 1001.
(61) Alessandri, R.; Souza, P. C. T.; Thallmair, S.; Melo, M. N.; de Vries, A. H.; Marrink, S. J. Pitfalls of the Martini Model. *J. Chem. Theory Comput.* **2019**, *15*, 5448−5460.
(62) Yoo, J.; Aksimentiev, A. Molecular Dynamics of Membrane-Spanning DNA Channels: Conductance Mechanism, Electro-Osmotic Transport, and Mechanical Gating. *J. Phys. Chem. Lett.* **2015**, *6*, 4680−4687.
(63) Ohmann, A.; Li, C.-Y.; Maffeo, C.; Al Nahas, K.; Baumann, K. N.; Göpfrich, K.; Yoo, J.; Keyser, U. F.; Aksimentiev, A. A Synthetic Enzyme Built from DNA Flips 107 Lipids per Second in Biological Membranes. *Nat. Commun.* **2018**, *9*, 2426.
(64) Sobota, D.; Joshi, H.; Ohmann, A.; Aksimentiev, A.; Keyser, U. F. Tailoring Interleaflet Lipid Transfer with a DNA-Based Synthetic Enzyme. *Nano Lett.* **2020**, *20*, 4306−4311.
(65) Padmanabha Das, K. M.; Shih, W. M.; Wagner, G.; Nasr, M. L. Large Nanodiscs: A Potential Game Changer in Structural Biology of Membrane Protein Complexes and Virus Entry. *Front. Bioeng. Biotechnol.* **2020**, *8*, 539.
(66) Doktorova, M.; Heberle, F. A.; Eicher, B.; Standaert, R. F.; Katsaras, J.; London, E.; Pabst, G.; Marquardt, D. Preparation of Asymmetric Phospholipid Vesicles for Use as Cell Membrane Models. *Nat. Protoc.* **2018**, *13*, 2086−2101.
(67) Macke, T. J.; Case, D. A. Modeling Unusual Nucleic Acid Structures. In *Molecular Modeling of Nucleic Acids; ACS Symposium Series*; American Chemical Society, 1997; Vol. *682*, pp 24−379.
(68) de Jong, D. H.; Singh, G.; Bennett, W. F. D.; Arnarez, C.; Wassenaar, T. A.; Schäfer, L. V.; Periole, X.; Tieleman, D. P.; Marrink, S. J. Improved Parameters for the Martini Coarse-Grained Protein Force Field. *J. Chem. Theory Comput.* **2013**, *9*, 687−697.
(69) Uusitalo, J. J.; Ingólfsson, H. I.; Akhshi, P.; Tieleman, D. P.; Marrink, S. J. Martini Coarse-Grained Force Field: Extension to DNA. *J. Chem. Theory Comput.* **2015**, *11*, 3932−3945.
(70) Berendsen, H. J. C.; van der Spoel, D.; van Drunen, R. GROMACS: A Message-Passing Parallel Molecular Dynamics Implementation. *Comput. Phys. Commun.* **1995**, *91*, 43−56.
(71) Abraham, M. J.; Murtola, T.; Schulz, R.; Páll, S.; Smith, J. C.; Hess, B.; Lindahl, E. GROMACS: High Performance Molecular Simulations through Multi-Level Parallelism from Laptops to Supercomputers. *SoftwareX* **2015**, *1−2*, 19−25.
(72) Berendsen, H. J. C.; Postma, J. P. M.; van Gunsteren, W. F.; DiNola, A.; Haak, J. R. Molecular Dynamics with Coupling to an External Bath. *J. Chem. Phys.* **1984**, *81*, 3684−3690.
(73) Bussi, G.; Donadio, D.; Parrinello, M. Canonical Sampling through Velocity Rescaling. *J. Chem. Phys.* **2007**, *126*, 014101−014107.
(74) de Jong, D. H.; Baoukina, S.; Ingólfsson, H. I.; Marrink, S. J. Martini Straight: Boosting Performance Using a Shorter Cutoff and GPUs. *Comput. Phys. Commun.* **2016**, *199*, 1−7.
(75) Verlet, L. Computer "Experiments" on Classical Fluids. I. Thermodynamical Properties of Lennard-Jones Molecules. *Phys. Rev.* **1967**, *159*, 98−103.
(76) Parrinello, M.; Rahman, A. Polymorphic Transitions in Single Crystals: A New Molecular Dynamics Method. *J. Appl. Phys.* **1981**, *52*, 7182−7190.
(77) Hunter, J. D. Matplotlib: A 2D Graphics Environment. *Comput. Sci. Eng.* **2007**, *9*, 90−95.
(78) Humphrey, W.; Dalke, A.; Schulten, K. VMD: Visual Molecular Dynamics. *J. Mol. Graphics* **1996**, *14*, 33−38.

https://dx.doi.org/10.1021/acsnano.0c07128
ACS Nano XXXX, XXX, XXX−XXX